Journal of Microscopy

Journal of Microscopy, Vol. 00, Issue 00 2017, pp. 1–10
Received 26 September 2016; accepted 1 March 2017

doi: 10.1111/jmi.12561

3D map distribution of metallic nanoparticles in whole cells using MeV ion microscopy

M.S. VASCO*, L.C. ALVES*,†, V. CORREGIDOR‡, D. CORREIA§, C.P. GODINHO§, I. SÁ-CORREIA§, A. BETTIOL‖, F. WATT‖ & T. PINHEIRO*,#

**Departamento de Engenharia e Ciências Nucleares, Instituto Superior Técnico, Universidade de Lisboa, Lisboa, Portugal*
†Centro de Ciências e Tecnologias Nucleares (C2TN), Instituto Superior Técnico, Universidade de Lisboa, Lisboa, Portugal
‡Instituto de Plasmas e Fusão Nuclear (IPFN), Instituto Superior Técnico, Universidade de Lisboa, Lisboa, Portugal
§Instituto de Bioengenharia e Biociencias (IBB), Departamento de Bioengenharia, Instituto Superior Técnico, Universidade de Lisboa, Lisboa, Portugal
‖Centre for Ion Beam Applications, Department of Physics, National University of Singapore, Singapore, Singapore
#Instituto de Bioengenharia e Biociências (IBB), Instituto Superior Técnico, Universidade de Lisboa, Lisboa, Portugal

Key words. 3D imaging, nanoparticles internalization, nuclear microscopy, Rutherford backscattering.

Summary

In this work, a new tool was developed, the MORIA program that readily translates Rutherford backscattering spectrometry (RBS) output data into visual information, creating a display of the distribution of elements in a true three-dimensional (3D) environment.

The program methodology is illustrated with the analysis of yeast *Saccharomyces cerevisiae* cells, exposed to copper oxide nanoparticles (CuO-NP) and HeLa cells in the presence of gold nanoparticles (Au-NP), using different beam species, energies and nuclear microscopy systems. Results demonstrate that for both cell types, the NP internalization can be clearly perceived. The 3D models of the distribution of CuO-NP in *S. cerevisiae* cells indicate the nonuniform distribution of NP in the cellular environment and a relevant confinement of CuO-NP to the cell wall. This suggests the impenetrability of certain cellular organelles or compartments for NP. By contrast, using a high-resolution ion beam system, discretized agglomerates of Au-NP were visualized inside the HeLa cell. This is consistent with the mechanism of entry of these NPs in the cellular space by endocytosis enclosed in endosomal vesicles. This approach shows RBS to be a powerful imaging technique assigning to nuclear microscopy unparalleled potential to assess nanoparticle distribution inside the cellular volume.

Introduction

Nanotechnology is now being applied in a multitude of areas, ranging from electronics and chemistry to food and textile production. Yet, the most fascinating application of nanotechnology resides in the biology field (Bondarenko *et al.*, 2013; Treuel *et al.*, 2013), and in particular at the cellular biology field, due to the scale in which the innumerable cellular functions operate.

Nanoparticles (NPs) can be used to probe cellular functions, shape physiological responses, vaccines and as biosensors (Mohanraj & Chen, 2006; Padmanabhan *et al.*, 2016; Torres-Sangiao *et al.*, 2016) among other applications, although the complete understanding of their biological toxicity remains unclear (Pujalt *et al.*, 2011; Chang *et al.*, 2012; Froehlich, 2015). Ongoing research on the biological effects of NP is being carried out, specifically on their quantization, transport and volume distribution in cells. To achieve these goals, high-resolution imaging techniques are essential. However, few are able to combine nanometre probe-formation with precise quantification of the elemental composition of an unknown matrix and the ability to examine the subsurface layers of a sample, retrieving the depth-dependent profile of those elements.

This is the prospect held by nuclear microscopy using focused MeV ion beams, usually hydrogen (^{1}H) and helium (^{4}He) ions, combining several ion beam analytical techniques in order to obtain submicro-sized 2 dimensional (2D) images of the sample morphology (STIM scanning transmission ion microscopy) and elemental distribution (PIXE - proton-induced X-ray emission) with depth information extracted from the calculated beam energy loss with Rutherford backscattering spectrometry (RBS) (Breese *et al.*, 1996; Watt *et al.*, 2011; Nastasi *et al.*, 2015; Jeynes & Colaux., 2016). Research using nuclear imaging techniques has been used to examine the biological consequences of the proliferation of NP (Gontier *et al.*, 2008; Godinho *et al.*, 2014) and to quantity and statistically estimate NP number in cells (Jeynes *et al.*, 2013; Le Trequesser *et al.*, 2014). Outstanding 20 nm spatial resolutions achieved

[Correction added on 10 May 2017, after first online publication: Authors "D. Correia, C.P. Godinho, I. Sá-Correia", originally omitted, has been added to the author list]

Correspondence to: Teresa Pinheiro, IBB - Instituto de Bioengenharia e Biociências, Instituto Superior Técnico, Av. Rovisco Pais 1, 1049 001 Lisboa, Portugal. Tel: +351 218419983; e-mail: teresa.pinheiro@tecnico.ulisboa.pt

by nuclear microprobes enabled the identification and quantization of gold NP and obtained direct evidence of the transport mechanism involved in the cellular entry of NP (Chen *et al.*, 2013). Providing submicrometre resolution ion beams and using multiple techniques, including RBS, the authors were able not only to differentiate between NP at the surface or inside the cell, but also to ascertain their depth distribution in the cellular environment. Thus, the nuclear microprobe techniques can then be a useful tool to study the interactions of NP with cells, a research topic fundamental for a safe widespread use of nanotechnology.

Although there are several software codes that enable precise sample point/area analysis and elemental depth profile retrieval, such as DAN32 (Grime, 1996), SIMNRA (Mayer, 2014) and DataFurnace (Barradas & Jeynes, 2008), visualization options of RBS data are not completely explored, especially concerning the elemental distribution in a fully three-dimensional (3D) environment. In order to tackle this problem, a new software code was developed and applied to the study of the 3D distribution of copper oxide nanoparticles (CuO-NP) in *Saccharomyces cerevisiae* cells and of gold nanoparticles (Au-NP) in a human cell line (HeLa cells).

3D model

Theoretical background

The underlying principles behind many of the different analytical techniques that use ion beams are the same. Initially, a beam of ions, with energy in the order of MeV, is aimed at the target, which will then penetrate the sample, losing energy along their trajectories, at a known rate, through collisions with nuclei and electrons. Due to these interactions, there is a probability ruled by the respective interaction cross-section, of emission of an output, which can then be detected, collected as a spectrum and analysed. This information can give precise details on the sample properties, such as atomic structure, matrix composition or elemental depth distribution.

The fundamental basis of RBS is the detection and analysis of the projectile ions that are backscattered after interacting with the nucleus of the elements that compose the sample matrix. This allows the identification of the elemental matrix of the sample, and the depth profile of those elements, as a consequence of the elastic collision between the incident ion and an atomic nucleus of the sample matrix, and the energy loss of the ion while traversing the sample, respectively. The interaction between the projectile ion and an atomic nuclei of the sample matrix can be thought as a two-body elastic collision between isolated particles: When the incident ion, of mass M_1, charge Z_1 and kinetic energy E_0, interacts with a target atom at rest, of mass M_2 and charge Z_2, the ion is scattered through an angle θ, with an atomic recoil angle of ϕ. The ratio of projectile energies after the interaction defines the kinematic factor K_{Target}, given by:

$$K_{\mathrm{Target}} = \frac{E_1}{E_0} = \left[\frac{[1-(M_1/M_2)^2\sin^2\theta]^{1/2} + M_1/M_2\cos\theta}{1+(M_1/M_2)}\right]^2. \quad (1)$$

Hence, for a known ion mass, the energy loss of the incident ion, after elastically colliding with the target atom, becomes a function only of the scattering angle θ and the target mass M_2 and thus the kinematic factor is the fundamental parameter of RBS analysis since, for a fixed θ, given by the detector position angle, it allows a precise identification of the unknown sample element. By contrast, the interaction of the innumerate ions of the beam with the atoms of the sample matrix is a statistical process, described as the elastic scattering of charge particles by the Coulomb interaction, giving rise to the Coulomb angular differential scattering cross-section, also known as the Rutherford differential cross-section which, in the laboratory frame of reference, is given by (Nastasi *et al.*, 2015):

$$\sigma_R = \frac{d\sigma(\theta)}{d\Omega} = \left(\frac{Z_1 Z_2 e^2}{4E}\right)^2 \frac{4}{\sin^4\theta} \frac{\{[1-((M_1/M_2)\sin\theta)^2]^{1/2}+\cos\theta\}^2}{[1-((M_1/M_2)\sin\theta)^2]^{1/2}} \quad (mb/sr). \quad (2)$$

With θ the scattering angle and E the projectile kinetic energy. The depth profiling ability of RBS is a consequence of the energy loss of the incident ions while traversing the sample before and after the elastic interaction with atomic nuclei, occurring prior to their detection. When an energetic ion traverses a material, it loses energy at a rate dE/dx, named stopping power, usually of a couple of hundred electron-Volt per nanometre, depending on the type of ion projectile (more precisely on M_1 and Z_1) and on the elemental matrix of the sample.

Depth profile model

The energy-loss process of ion projectiles occurs in three different stages: first, the ions continuously lose energy through interactions with the electrons of the atoms as they traverse the sample, until elastically colliding with the nucleus of a given element, losing a fraction K_{Target} of its energy, after which the ions, once again, successively lose energy through electronic interactions before emerging from the sample (Fig. 1).

The stopping cross-section for a given element in a multi-elemental sample ($[\epsilon]_A^{AB}$) can be given by:

$$[\epsilon]_A^{AB} = \left(K_A \epsilon_{\mathrm{in}}^{AB} \frac{1}{\cos\theta_1} + \epsilon_{\mathrm{out}}^{AB} \frac{1}{\cos\theta_2}\right), \quad (3)$$

where θ_1 and θ_2 are the angles defined in Figure 1 and the stopping powers are those of the ion before and after the interaction with the nucleus. It is possible to define a depth resolution δt, the minimum detectable difference in depth, which is related to the minimum energy difference detectable by the experimental

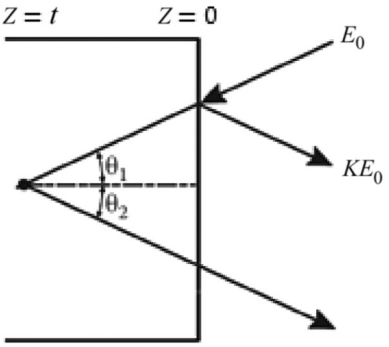

Fig. 1. Kinematics of the energy loss mechanism of an ion beam of energy E_0, until its interaction with the nucleus of an element Z of the sample at a depth t. θ_1 and θ_2 are the incident and backscattered angles. Adapted from Nastasi *et al.* (2015).

apparatus δE (the particle detector energy resolution), such that:

$$\delta t = \frac{\delta E}{[\epsilon]}. \quad (4)$$

For thin films ($t < 100$ nm), using common ion species for the beam, the relative change in the value of ϵ along the projectile trajectory is small. In other words, the relative change of the projectile energy is small, and the evaluation can be carried out using the 'surface energy approximation', in which ϵ is evaluated at the energy before and after an elastic collision with a target nucleus at the sample surface, E_0 and $K E_0$, respectively:

$$[\epsilon_0] = \left[K_{\text{Target}}\, \epsilon(E = E_0) \frac{1}{\cos\theta_1} + \epsilon(E = K E_0) \frac{1}{\cos\theta_2} \right]. \quad (5)$$

Material and methods

Saccharomyces cerevisiae growth condition

The parental *S. cerevisiae* strain BY4741 was used in this work. Cell cultivation followed previously described protocols (Fernandes & SáCorreia, 2001; Gil *et al.*, 2015). Briefly, cells were grown at 30°C with orbital agitation (250 rpm) in minimal growth medium MM4, containing per litre: 1.7 g yeast nitrogen base without amino acids, 2.65 g $(NH_4)_2SO_4$ (Panreac, Spain), 20 g glucose (Merck, Germany), 20 mg L-histidine (Merck, Germany), 20 mg L-methionine (Merck, Germany), 60 mg L-leucine (Sigma-Aldrich, USA) and 20 mg L-uracil (Sigma-Aldrich, USA). Cell cultures were supplemented with CuO-NP (CuO 99% with a relation of 0.2248 gCu/gNP, nominal size 30–50 nm, Nanostructured & Amorphous Materials, Inc., Houston, USA) in order to obtain a medium concentration of 40 mg Cu/L. The CuO-NPs were previously suspended in 18 MΩ.cm ultrapure water (Milli-Q Element, Darmstadt, Germany). Cell growth and viability were followed, by measuring colony-forming units counts repeatedly during at least 24 h.

Sample preparation for nuclear microscopy

Samples were prepared from cell aliquots taken at incubation point in time corresponding to the exponential growth phase. Cells were washed in double distilled water by centrifugation at 2500 rpm during 5 min to remove excess CuO-NP in the culture medium. Cells were resuspended in 100 μL of water and 5 μL of the cell suspension rapidly deposited on a 1.5 μm polycarbonate foil, quench-frozen at –80°C to assure cell integrity (Minqin *et al.*, 2007; Pinheiro *et al.*, 2007; Pinheiro *et al.*, 2013). Cells were allowed to dry at –25°C in a cryostat before analysis.

Nuclear microscopy/nuclear microprobe

The analysis was conducted using the nuclear microprobe (OM 150 triplet system, Oxford Microbeams Ltd., UK) installed at one of the beam lines of the 2.5 MV Van de Graaff accelerator at IST-CTN (Alves *et al.*, 2000; Veríssimo *et al.*, 2007). With a beam spatial resolution of 3×4 μm^2, for an average 100 pA current, the equipment contains a dipolar magnetic system for beam deflection, responsible for scanning the beam over the sample surface in 256×256 steps, encompassing a maximum area of 2.6×2.6 mm^2 for 2 MeV protons. The samples are contained in an experimental vacuum chamber, also accommodating an X-ray detector for PIXE, a Si PIN diode for STIM and an RBS surface-barrier Si detector, with 20 keV of energy resolution, positioned at a backward angle of 40° with the beam direction (Cornell geometry). In this work, STIM in off-axis geometry was used, allowing the simultaneous use of PIXE and RBS techniques (Aguer *et al.*, 2005). Basic data acquisition and manipulation, including creation of 2D elemental maps, is done using the OMDAQ software (Version 1.3.71.725, 2007 (Oxford Microbeams, Ltd., UK)), which also includes DAN32 software (Oxford Microbeams, Ltd., UK) for offline RBS spectra analysis (Grime & Dawson, 1995).

The MORIA software

The MORIA (Micro-beam RBS Image Analyser) program is a C++ coded software that enables the presentation of the model of the distribution of a given sample element, in a fully 3D environment, and the interaction with the model in real time. MORIA combines an automated input file processing with a user-friendly graphical interface, developed using the wxWidgets toolkit (Version 3.1.0, 2016), which allows setting up the different aspects of the simulation and a fast and efficient 3D renderer, taking advantage of the VTK package (Version 6.3.0, 2006). The procedures of the program are described in Figure 2.

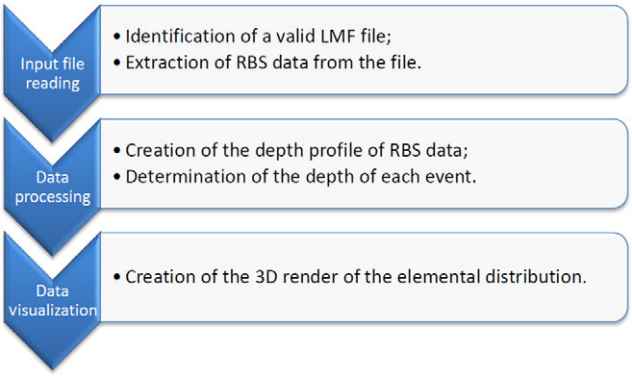

Fig. 2. Pipeline of the MORIA software.

- *Input file reading*
  The allowed input file type of MORIA is the OMDAQ's List-mode (LMF) file type, which is a collection of event-by-event data, stored in N blocks of information, each containing the energy of the detected event as well as the position of the beam over the sample at the moment of detection. Each RBS event is stored in the program and subsequently processed. The program is able to take into account the full range of beam positions (256×256 for CTN microprobe, or higher). To increase the event counting statistics in RBS analysis, subpar visualization is also implemented, storing the events in a 2D 64×64 vector of structures. The software also retrieves various types of experimental and formatting information contained in several header blocks of the LMF file, which are crucial for subsequent data processing.
- *Data processing*
  At this point in the analysis, the user must insert not only the sample matrix, but also define the analysis limits, through the selection of the element to be modelled (K_{Target}) and the element whose surface barrier in RBS spectrum corresponds to the lower energy limit of the analysis (K_{Limit}). The values of atomic charge and mass for both elements are automatically assigned from the existent database in the program, and the values of their surface barriers are determined, taking into account the experimental configuration. After this process, the energy loss of the ion beam in the sample is evaluated using the 'surface-energy approximation' (Eq. (5)), taking into account the inserted biological matrix. As such, for each valid event, accordingly to the user-selected analysis limits, its absolute depth is determined and subsequently sorted into depth layers, of initial width given by the depth resolution of the system (Eq. (4)), thus incrementing the number of events in each depth layer with (x,y) coordinates. At the end of this sorting process, in order to better represent the concentration of the modelled element in the sample space, the number of events in each depth layer is corrected, taking into account the variation of cross-section along the sample. The used stopping power and differential cross-section elemental values were obtained from available computational codes and databases such as SigmaCalc (Gurbich, 2010) and SRIM (Ziegler *et al.*, 2010).
- *Data visualization*
  Finally, the 3D model of the distribution of the user-selected element in the sample is created, using the VTK rendering package. The model of a given element in MORIA is composed of a 3D vector of cubic source data objects, in number equal to the number of nonnull entries of depth layers. Their surface dimensions are taken accordingly to the scan size of the experimental run and the depth dimension is magnified by a factor of 10, for a better onscreen visualization. The information regarding the number of events in each depth layer of the model is given through a rainbow colour mapping of each cubic data object. After the creation of the cubic source objects, the program uses the standard chain of objects for VTK visualization. The created elemental model in MORIA may be zoomed, rotated and spatially translated in real time by the user. The MORIA program also includes several functions to interact with the model in order to assist the analysis, such as changing the resolution or the number of depth layers of the model, visualize element depth distributions of the model along a user- defined transversal plane or creating secondary elemental models, superimposed in the original model space. For a detailed discussion of the implementation of VTK in MORIA and its analysis functions, please refer to (Vasco, 2016).

Results

In order to validate the model, different applications of MORIA are presented, regarding the creation of 3D models of the depth distribution of nanoparticles in biological samples: copper oxide nanoparticles (CuO-NP) in *S. cerevisiae* and gold nanoparticles (Au-NP) in *HeLa* cells.

S. cerevisiae cells

The analysis of *S. cerevisiae* cells exposed to CuO-NP was conducted using the microbeam facility available at IST-CTN. Typically, cells were irradiated for approximately 1 h, applying both 2.0 MeV ^{1}H and ^{4}He ion beams, in order to assess the potential of each ion type for imaging purposes.

To construct the model of the distribution of the CuO-NP in cells, it becomes necessary to initially determine the composition of the biological matrix of each cell through the simulation and fit of RBS spectra representative of cells, as presented in Figure 3.

The obtained sample matrix serves as an input to MORIA. The upper limit of analysis was taken as the element to be modelled (K_{Target}) and the lower limit (K_{Limit}) as the highest Z element relevant to the biological matrix, which for cells

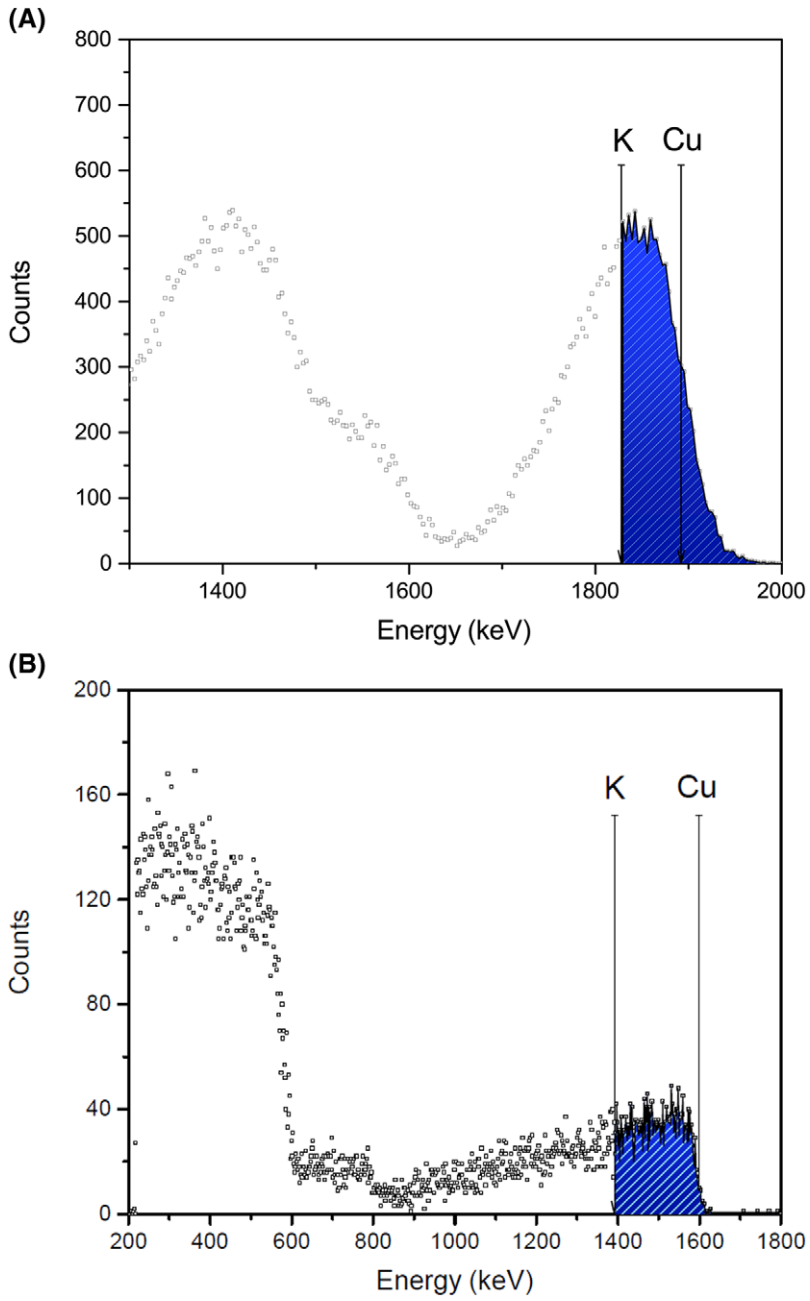

Fig. 3. RBS spectra of the *Saccharomyces cerevisiae* samples conducted using ^{1}H ions (A) and ^{4}He ions (B), along with the section used in MORIA analysis in blue, defined by the surface barrier of the chosen limit elements.

commonly refers to K. Using the MORIA software, the model parameters for the energy depth calibration t_E, expressed in keV/nm, and the maximum depth probed t^{Max} can be calculated. The user input and program calculated parameters for the analysis of the *S. cerevisiae* individual cells in MORIA are presented in Table 1. The calculation of the number of layers takes into account the energy loss of the projectile in the sample and the depth resolution of the system.

As can be inferred from Table 1, the calculated parameters differ considerably with the selection of ion beam species. Due to their reduced energy loss in the sample, ^{1}H ion analysis is able to probe further in the sample, at a cost of a lower experimental depth resolution, and thus a lower maximum number of depth layers. By contrast, the significant increase in the energy loss of ^{4}He ions in the sample translates into an increase in the depth resolution of the system, followed by

Table 1. MORIA user input and program calculated parameters for the analysis of the *Saccharomyces cerevisiae* samples, using H and He ions.

MORIA	^{1}H	^{4}He
K_{Target}	Cu ($M_2 = 63.5, Z_2 = 29$)	Cu ($M_2 = 63.5, Z_2 = 29$)
K_{Limit}	K ($M_2 = 39.1, Z_2 = 19$)	K ($M_2 = 39.1, Z_2 = 19$)
t_E (keV/nm)	0.061	0.590
t^{Max} (nm)	1011	344
# Depth layers	4	11

an increase in the number of depth layers, in detriment of a shallower depth probed by the model.

The renders of the created models are presented in Figure 4. For better visualization of the cell morphology and contour, the STIM map (Figs. 4 A, D), obtained simultaneously to RBS and PIXE data, was also used. The distribution of Cu in the cells, presented in Figures 4(B) and (E), reveals a significant uptake of this element by the cell. This was confirmed with the distribution of Cu derived from CuO-NP shown in Figures 4(C) and (F) obtained along a sample cross-section cut (along the dashed line indicated in Figs. 4B and E), which could give new insight into the issue of the NP entry mechanisms in *S. cerevisiae*, currently fully unresolved (Kasamets *et al.*, 2013).

HeLa cells

In order to access the effects of the usage of a high-resolution microbeam setup for RBS imaging, a sample of HeLa cells in the presence of Au-NP that were deposited on top of a silicon nitride window was analysed. The analysis was conducted in the Centre for Ion Beam Applications at the National University of Singapore (CIBA@NUS), which used a 300 nm spot sized ^{4}He beam and whose output analysis file was kindly provided by the group. For a complete description of the experimental setup used, please refer to (Bettiol *et al.*, 2009; Chen *et al.*, 2013).

The biological matrix of the sample was determined using the fit of the RBS spectrum of an area mask representative of the cell. The analysis of HeLa cells in MORIA, following the methodology introduced before, is presented in Table 2,

Table 2. MORIA user input and program calculated parameters for analysis of the HeLa sample.

MORIA	^{4}He
K_{Target}	Au ($M_2 = 197, Z_2 = 79$)
K_{Limit}	Si ($M_2 = 28.1, Z_2 = 14$)
t_E (keV/nm)	0.502
t^{Max} (nm)	892
# Depth layers	23

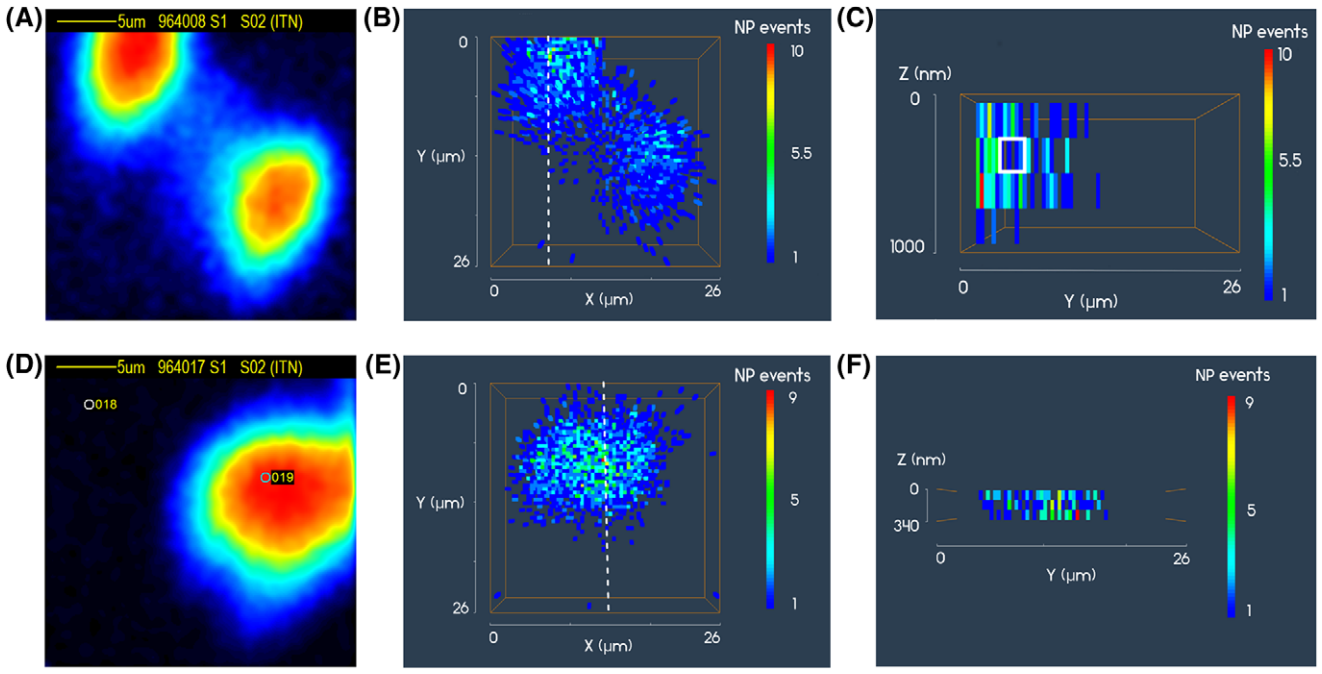

Fig. 4. Top panel: (A) STIM image of *Saccharomyces cerevisiae* cells using a 2.0 MeV ^{1}H beam, for a scanned area of 26×26 µm^2; (B) MORIAs 64×64 3D model of the distribution of Cu in the two yeast cells, for the analysis conditions in (A); (C) cross-section cut of the depth distribution of Cu in the top cell, along the line shown in (B), highlighting a significant uptake of Cu by the cell. Bottom panel: (D) STIM image of the analysis *Saccharomyces cerevisiae* sample using a 2.0 MeV ^{4}He beam, for a scanned area of 26×26 µm^2; (E) MORIAs 64×64 3D model of the distribution of Cu in the same sample and for the same analysis conditions in (D); (F) cross-section cut of the depth distribution of Cu in the cell, along the line shown in (F).

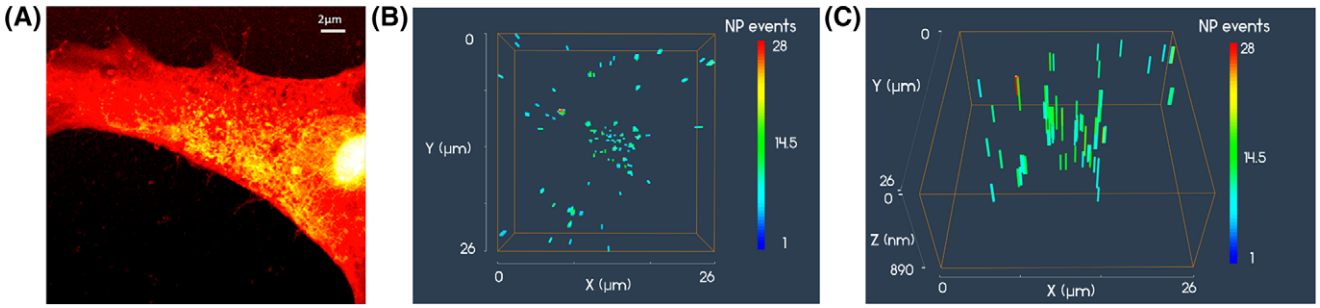

Fig. 5. (A) STIM image of the HeLa sample analysis, conducted using a 1.6 MeV ^{4}He beam (adapted from Chen *et al.*, 2013); (B) MORIAs 128×128 3D model of the distribution of Au in the HeLa sample, for a 1.6 MeV ^{4}He beam; (C) tilted view of the depth distribution of Au in the cell, highlighting the discrete distribution of the AuNP in the cell.

along with the created distributions, presented in Figure 5. As evident in the elemental model (Fig. 5B), the use of a higher resolution beam allows the increase in the resolution of the model. As can be extracted from Eq. (1), the analysis of a higher than copper Z element, such as gold, allows a better separation between the surface barrier of the limit elements (K_{Target} and K_{Limit}), resulting in a higher depth probed without interference of the sample matrix, even for similar depth resolution and projectile energy loss. Consequently, the maximum number of depth layers is also increased. Also notice that the $(Z_2)^2$ dependence of the scattering cross-section (Eq. (2)) reduces the cell elemental contribution to the RBS spectrum when gold NPs are analysed instead of Cu NP.

The distribution of Au-NP along and inside the cell is not uniform, occurring in discrete agglomerates, which are clearly visualized in this higher resolution model (Fig. 5B) Moreover, the results obtained translate depth information in a fully 3D environment, consistent with results previously published (Chen *et al.*, 2013), where depth intervals were obtained using sections of the RBS spectrum.

Volume rendering

The MORIA program allows the simultaneous creation of a secondary model, superimposed in the sample space along with the main elemental distribution, e.g. Au or Cu containing NP as shown in our study. The creation of the secondary model relies on the careful definition of energy limits corresponding to signature elements of the specimen (e.g. physiological elements). This secondary model produces an approximate representation of the volume enclosed by the cell. The biological volumes of the *S. cerevisiae* sample analysed with ^{1}H ion beam and of the HeLa with ^{4}He beam are presented in Figure 6.

Both volume models correctly match their 2D representation, obtained through STIM analysis. A limitation of this representation derives from the difficulty of defining unique elemental signatures for cell limits, as main physiological elements are also commonly present in the extra-cellular medium. Still, this methodology presents itself as an advantage over simple 2D image overlay, since it is able to give a simplistic representation of the objects volume superimposing the NP distribution in 3D, which is fundamental for the

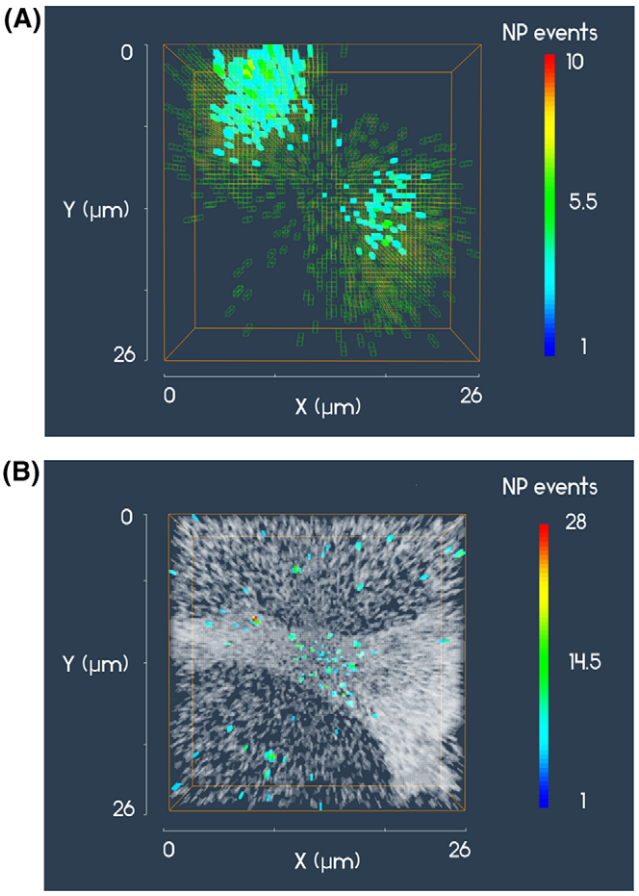

Fig. 6. Representation of the cellular volumes using a secondary model based on selected element surface barrier energy limits of physiological elements (transparent white) superimposed in the sample space with the main elemental distribution of CuO or AuNP (bright blue). (A) Volume rendering of the *Saccharomyces cerevisiae* sample analysis using ^{1}H ions and (B) volume rendering of the HeLa sample analysis using ^{4}He ions.

interpretation of the profile information of the element of interest, given by the main elemental model.

Discussion

The core focus of this study was the development of a new tool that readily translates RBS technique output data into visual information. The new developed MORIA program takes advantage of the focused MeV ion beam analytical capabilities and the ideal RBS case study type (heavy element in a light matrix) to assess depth distribution of Cu or Au nanoparticles in a biological matrix, accounting for the energy loss and the changing cross-section along the projectile path in the sample. Therefore, MORIA can display the semiquantitative elemental distribution in a fully 3D environment. In spite of its high potential for 3D image reconstruction, accessing a general RBS case is still a complex and unsolved problem as recently reviewed by (Jeynes & Colaux, 2016). The simplicity of the 3D imaging attained with MORIA, requiring simple experimental setup, sample stage holders and reasonable data collection time (1 h), contrasts with IBA tomographic modalities. Tomographic 3D images obtained using PIXE and STIM techniques (Michelet *et al.*, 2015) require harder sample preparation, precise translation and rotation sample stage, as well as longer data acquisition and computer processing times.

As previously stated, the MORIA software includes several functions to complement the analysis, such as changing the resolution or the number of depth layers of the model. Model image resolution/quality predictably depends on the nuclear microprobe beam spatial resolution attained (system dependent) and on the depth resolution/discrimination possible to define which is a function of the particle detector energy resolution, sample composition and on the species and energy of the ion beam used. Although the program is functional, future upgrades of the program must address some inadequacies in its methodology particularly in what concerns a more precise calculation of the energy loss in the sample, which currently resorts to the surface-energy approximation. This new implementation would improve the quality of 3D elemental images, as more precise calculations of backscattering spectrometry data can be introduced by upgrading to improved software tools, such as the DataFurnace code (Barradas & Jeynes, 2008) to obtain depth profile information per pixel for relevant matrix constituents. The current existent limitation in most of the nuclear microprobe setups is statistical power due to limited resistance of the biological material to beam irradiation damage and to the low amount in the sample of the element of interest. However, combining the RBS signal with the PIXE information could be an interesting possibility to render quantitative 3D images of complex samples, as previously suggested (Bird, 1990; Jeynes & Colaux, 2016).

The program methodology was illustrated with the analysis of whole yeast *S. cerevisiae* cells, exposed to CuO-NP and HeLa cells in the presence of Au-NP, using different beam species, energies and nuclear microscopy systems. The choice of the beam species becomes a function of the purpose of the analysis: the inspection of surface and subsurface sample volumes with high depth resolution, in the order of tens of nanometres, using ^{4}He ions, or a more global analysis of the distribution of a given element in the sample, using ^{1}H ions.

Results demonstrate that for both cell types, the NP internalization can be clearly perceived.

The 3D models of the distribution of Cu in *S. cerevisiae* cells, either using ^{1}H or ^{4}He to adjust depth resolution and micrometre beam dimension, revealed that the NP intake of the cells was significant. Yet, the distribution inside the cells exhibits volumes where the presence of NP was considerably low, which indicates the nonuniformity of their distribution in the cellular environment and a relevant confinement to the cell surface or to the cellular wall, a suggestion of the impenetrability of certain cellular organelles or compartments for NP.

When a high-resolution MeV ^{4}He ion beam is used (Chen *et al.*, 2013), such as in the analysis of the HeLa cell, the 3D model created with MORIA enabled both the definition and positioning of agglomerates of Au-NP in the sample space. The rendered model discretized agglomerates of Au-NP in the cell, which is indeed consistent with their mechanism of entry in the cellular space by endocytosis (Iversen *et al.*, 2011), enclosed in endossomal vesicles, as discussed by Chen *et al.* (2013).

The results obtained with the two systems clearly show the strong influence of beam size in the quality assessment of the analysis. The distribution of Au-NP in the HeLa cell can be discretized, whereas in *S. cerevisiae,* the Cu distribution was apparently continuous. In the experiment with CuO-NP the attained spacial beam resolution clearly hinders the ability to assert the level of impenetrability of organelles for NP and to discriminate CuO-NP agglomerates. Nevertheless, even under these conditions, which are routinely available in every microbeam setup, it is possible to create 3D models representative of the penetration of NP in cells. In higher resolution setups, quantization and quantification of NP in whole cell volume become possible.

Currently, transmission electron microscopy (TEM) is considered the gold standard for the localization of electron dense NP within a cell and in specific compartments. Spatial resolution offered is unbeatable, which allows resolving single NP from agglomerates. However, TEM requires laborious sample preparation with the use of resin-embedded samples and the analysis is restricted to ultra-thin sections of the cell, rising representativeness issues. Through sequential cross-section observation, it is possible to understand the 3D distribution of NP within a defined reference volume (Brandenberger *et al.*, 2010) following elaborated sampling schemes that can provide unbiased information on NP number, length, surface and volume in 3D from 2D images (Nyengaard & Gundersen, 2006). Scanning electron microscopy (SEM) link high-resolution images

to the possibility of inspecting the interactions of NP with biological systems as cryo-fixed cells can be directly analysed (Plascencia-Villa *et al.*, 2012). Hyphenation of SEM with other techniques, such as high-resolution focused ion beam milling and X-ray fluorescence, has allowed 3D distribution and composition of metal oxide NP postinternalization, by producing a series of ablate material from the cell surface where elemental distributions can be assessed (James *et al.*, 2013). However, these techniques tend to be intricate, time- and resource-consuming. They also rely on indirect 3D reconstruction using mathematical codes that may introduce artefacts.

Optical microscopy modalities based on fluorescently tagged NP, such as confocal laser scanning microscopy and fluorescent correlation spectroscopy, are relatively more simple alternatives to study NP interactions in either live or fixed cells (Fleischer & Payne, 2014). The drawback of these approaches, besides the limited axial resolution in specimens thicker than the focal point and fluorophore bleaching, is NP surface manipulation that inevitably will modify NP corona formation in physiological medium and eventually their mode of action (Tenzer *et al.*, 2013). Therefore, the departure of NP from their pristine state in the biological environment, which is fundamental to understand mechanisms of NP interaction with cells, is hindered.

As demonstrated in this paper, nuclear microscopy is a powerful way to get information about the NP interactions with cells. The new imaging modality based on RBS technique assigns to nuclear microscopy unparalleled specimen 3D visualization possibilities. Moreover, depth resolutions of 40 nm can now be added to the submicrometre spatial resolution achieved in 2D images. Besides, it is possible to analyse cryo-fixed specimens close to their native state, without any cell fixation or contrast use, therefore keeping the cellular morphology (Minqin *et al.*, 2007; Pinheiro *et al.*, 2007; Gontier *et al.*, 2008). This is essential to combine cell morphological details with NP distribution in the 3D cell space and assure any NP compartmentalization. These capabilities represent a high potential in studies dealing with the interaction of engineered NP with cells, in controlled conditions close to physiological state, which is a research topic fundamental for unravelling NP mechanisms of action and eventually for ensuring their safe use (Bondarenko *et al.*, 2013; Tenzer *et al.*, 2013; Wang *et al.*, 2014; Padmanabhan *et al.*, 2016; Torres-Sangiao *et al.*, 2016).

Conclusions

The new software tool, MORIA, takes advantage of the focused MeV ion beam analytical capabilities existent in nuclear microscopy systems, in particular of RBS, to assess depth distribution of a chosen heavy element in the whole cellular space and displaying it into visual information in 3D.

The obtained models of the distribution of CuO-NP and Au-NP inside cells clearly demonstrated the potential of this new image modality in ensuring NP compartmentalization while displaying NP in a true 3D environment.

During recent years, a collection of techniques have been developed and optimized to detect NP, locate the specific compartment and quantify the total number of intracellular NP at the single cell level. The reported advancement in nuclear microscopy, which expands traditional 2D views with system-dependent spatial resolution to fully 3D sample volumes depiction with 40 nm depth resolution, shows unique advantages of this technique in the study of NP interaction with cells. Also, due to the minimal sample preparation required, nuclear microscopy can then be a useful tool to assess the acquisition of intracellular NP quantities, their localization in specific compartments, and contribute to unravel key cellular mechanisms of NP binding, uptake and transport.

Acknowledgements

This study was supported by Fundação para a Ciência e Tecnologia (FCT) (UID/BIO/04565/2013 and UID/Multi/04349/2013 contracts) and Programa Operacional Regional de Lisboa, POR Lisboa 2020 (LISBOA-01-0145-FEDER-007317 contract). The work performed in CIBA is supported by the Ministry of Education - Singapore, Academic Research Fund Tier 2 grant (R-144-000-306-112).

References

Aguer, P., Alves, L.C., Barberet *et al.* (2005) Skin morphology and layer identification using different STIM geometries. *Nucl. Instr. Meth. Phys. Res.* **231**(1), 292–299.

Alves, L.C., Breese, M.B.H., Alves, E. *et al.* (2000) Micron-scale analysis of SiC/SiC f composites us-ing the new Lisbon nuclear microprobe. *Nucl. Instr. Meth. Phys. Res.* **161**, 334–338.

Barradas, N.P. & Jeynes, C. (2008) Advanced physics and algorithms in the IBA DataFurnace. *Nucl. Instr. Meth. Phys. Res.* **266**(8), 1875–1879.

Bettiol, A.A., Udalagama, C. & Watt, F. (2009) A new data acquisition and imaging system for nuclear microscopy based on a Field Programmable Gate Array card. *Nucl. Instr. Meth. Phys. Res.* **267**(12), 2069–2072.

Bird, J.R. (1990) Total analysis by IBA. *Nucl. Instr. Meth. Phys. Res.* **45**(1), 514–518.

Bondarenko, O., Juganson, K., Ivask, A., Kasemets, K., Mortimer, M. & Kahru, A. (2013) Toxicity of Ag, CuO and ZnO nanoparticles to selected environmentally relevant test organisms and mammalian cells in vitro: a critical review. *Arch. Toxicol.* **87**(7), 1181–1200.

Brandenberger, C., Mühlfeld, C., Ali, Z. *et al.* (2010) Quantitative evaluation of cellular uptake and trafficking of plain and polyethylene glycol-coated gold nanoparticles. *Small* **6**(15), 1669–1678.

Breese, M.B., Jamieson, D.N. & King, P.J. (1996) *Materials Analysis Using a Nuclear Microprobe*. John Wiley & Sons Ltd, Chichester, UK.

Chang, Y.N., Zhang, M., Xia, L., Zhang, J. & Xing, G. (2012) The toxic effects and mechanisms of CuO and ZnO nanoparticles. *Materials* **5**(12), 2850–2871.

Chen, X., Chen, C.B., Udalagama, C. *et al.* (2013) High-resolution 3D imaging and quantification of gold nanoparticles in a whole cell using scanning transmission ion microscopy. *Biophys. J.* **104**(7), 1419–1425.

Fernandes, A.R. & Sá Correia, I. (2001) The activity of plasma membrane H+ATPase is strongly stimulated during *Saccharomyces cerevisiae* adaptation to growth under high copper stress, accompanying intracellular acidification. *Yeast* **18**(6), 511–521.

Fleischer, C.C. & Payne, C.K. (2014) Nanoparticlecell interactions: molecular structure of the protein corona and cellular outcomes. *Acc. Chem. Res.* **47**(8), 2651–2659.

Froehlich, E. (2015) Value of phagocyte function screening for immunotoxicity of nanoparticles in vivo. *Int. J. Nanomed.* **10**, 3761–3768.

Gil, F.N., Moreira-Santos, M., Chelinho, S. *et al.* (2015) Suitability of a *Saccharomyces cerevisiae*-based assay to assess the toxicity of pyrimethanil sprayed soils via surface runoff: comparison with standard aquatic and soil toxicity assays. *Sci. Total Environ.* **505**, 161–171.

Godinho, R.M., Cabrita, M.T., Alves, L.C. & Pinheiro, T. (2014) Imaging of intracellular metal partitioning in marine diatoms exposed to metal pollution: consequences to cellular toxicity and metal fate in the environment. *Metallomics* **6**(9), 1626–1631.

Gontier, E., Ynsa, M.D., Bíró, T. *et al.* (2008) Is there penetration of titania nanoparticles in sunscreens through skin? A comparative electron and ion microscopy study. *Nanotoxicology* **2**(4), 218–231.

Grime, G.W. (1996) The Q factor method: quantitative microPIXE analysis using RBS normalisation. *Nucl. Instr. Meth. Phys. Res.* **109**, 170–174.

Grime, G.W. & Dawson, M. (1995) Recent developments in data acquisition and processing on the Oxford scanning proton microprobe. *Nucl. Instr. Meth. Phys. Res.* **104**(1), 107–113.

Gurbich, A.F. (2010) Evaluated differential cross-sections for IBA. *Nucl. Instr. Meth. Phys. Res.* **268**(11), 1703–1710.

Iversen, T.G., Skotland, T. & Sandvig, K. (2011) Endocytosis and intracellular transport of nanoparticles: present knowledge and need for future studies. *Nano Today* **6**(2), 176–185.

James, S.A., Feltis B.N., D. de Jonge, M. *et al.* (2013) Quantification of ZnO nanoparticle uptake, distribution, and dissolution within individual human macrophages. *ACS Nano* **7**(12), 10621–10635.

Jeynes, C. & Colaux, J.L. (2016) Thin film depth profiling by ion beam analysis. *Analyst* **141**(21), 5944–5985.

Jeynes, J.C.G., Jeynes, C., Merchant, M.J. & Kirkby, K.J. (2013) Measuring and modelling cell-to-cell variation in uptake of gold nanoparticles. *Analyst* **138**(23), 7070–7074.

Kasemets, K., Suppi, S., Künnis-Beres, K. & Kahru, A. (2013) Toxicity of CuO nanoparticles to yeast *Saccharomyces cerevisiae* BY4741 wild-type and its nine isogenic single-gene deletion mutants. *Chem. Res. Toxicol.* **26**(3), 356–367.

Le Trequesser, Q., Devès, G., Saez G. *et al.* (2014) Single cell in situ detection and quantification of metal oxide nanoparticles using multimodal correlative microscopy. *Anal. Chem.* **86**(15), 7311–7319.

Mayer, M. (2014) Improved physics in SIMNRA 7. *Nucl. Instr. Meth. Phys. Res.* **332**, 176–180.

Michelet, C., Barberet, P., Moretto, P. & Seznec, H. (2015) Development and applications of STIM-and PIXE-tomography: a review. *Nucl. Instr. Meth. Phys. Res.* **363**, 55–60.

Minqin, R., van Kan, J.A., Bettiol, A.A. *et al.* (2007) Nano-imaging of single cells using STIM. *Nucl. Instr. Meth. Phys. Res.* **260**(1), 124–129.

Mohanraj, V.J. & Chen, Y. (2006) Nanoparticles: a review. *Trop. J. Pharm. Res.* **5**(1), 561–573.

Nastasi, M., Mayer, J.W. & Wang, Y. (2015) *Ion Beam Analysis: Fundamentals and Applications*. CRC Press, Boca Raton, USA.

Nyengaard, J.R. & Gundersen, H.J.G. (2006) Direct and efficient stereological estimation of total cell quantities using electron microscopy. *J. Microsc.* **222**(3), 182–187.

OMDAQ. (2007) Computer software. Retrieved from http://www.microbeams.co.uk (March, 2017).

Padmanabhan, P., Kumar, A., Kumar, S., Chaudhary, R.K. & Gulyás, B. (2016) Nanoparticles in practice for molecular-imaging applications: an overview. *Acta Biomaterialia* **41**(1) 1–16.

Pinheiro, T., Moita, L., Silva, L., Mendonça, E. & Picado, A. (2013) Nuclear microscopy as a tool in TiO2 nanoparticles bioaccumulation studies in aquatic species. *Nucl. Instr. Meth. Phys. Res.* **306**, 117–120.

Pinheiro, T., Pallon, J., Alves, L.C. *et al.* (2007) The influence of corneocyte structure on the interpretation of permeation profiles of nanoparticles across skin. *Nucl. Instr. Meth. Phys. Res.* **260**(1), 119–123.

Plascencia-Villa, G., Starr, C.R., Armstrong, L.S., Ponce, A. & Jos-Yacamán, M. (2012) Imaging interactions of metal oxide nanoparticles with macrophage cells by ultra-high resolution scanning electron microscopy techniques. *Integr. Biol.* **4**(11), 1358–1366.

Pujalté, I., Passagne, I., Brouillaud, B. *et al.* (2011) Cytotoxicity and oxidative stress induced by different metallic nanoparticles on human kidney cells. *Part. Fibre Toxicol.* **8**(10), 1–16.

Tenzer, S., Docter, D., Kuharev, J. *et al.* (2013) Rapid formation of plasma protein corona critically affects nanoparticle pathophysiology. *Nat. Nanotechnol.* **8**(10), 772–781.

Torres-Sangiao, E., Holban, A.M., Gestal, M.C. (2016) Advanced nanobiomaterials: vaccines, diagnosis and treatment of infectious diseases. *Molecules* **21**(7), 867–889.

Treuel, L., Jiang, X. & Nienhaus, G.U. (2013) New views on cellular uptake and trafficking of manufactured nanoparticles. *J. Roy. Soc. Interface* **10**, 20120939, 1–22.

Vasco, M. (2016) *3D map of the distribution of metals in a cell: applications to the toxicity of nanoparticles*. Master Thesis, Instituto Superior Técnico, Universidade de Lisboa. Available at http://www.goo.gl/Nm7VR2 (June, 1st 2016).

Veríssimo, A., Alves, L.C., Filipe, P. *et al.* (2007) Nuclear microscopy: a tool for imaging elemental distribution and percutaneous absorption in vivo. *Microsc. Res. Techn.* **70**(4), 302–309.

VTK. (2006) Computer software. Retrieved from http://www.vtk.org (January, 5th 2016).

Wang, E.C. & Wang, A.Z. (2014) Nanoparticles and their applications in cell and molecular biology. *Integr. Biol.* **6**(1), 9–26.

Watt, F., Chen, X., De Vera, A.B. *et al.* (2011) The Singapore high resolution single cell imaging facility. *Nucl. Instr. Meth. Phys. Res.* **269**(20), 2168–2174.

wxWidgets. (2016) Computer software. Retrieved from http://www.wxwidgets.org (January, 5th 2016).

Ziegler, J.F., Ziegler, M.D. & Biersack, J.P. (2010) SRIM – the stopping and range of ions in matter. *Nucl. Instr. Meth. Phys. Res.* **268**(11), 1818–1823.